coatings

MDPI

Review

Structural Changes of Hydroxylapatite during Plasma Spraying: Raman and NMR Spectroscopy Results

Robert B. Heimann

Am Stadtpark 2A, D-02826 Görlitz, Germany; robert.heimann@ocean-gate.de; Tel.: +49-3581-667851

Abstract: Functional osseoconductive coatings based on hydroxylapatite (HAp) and applied preferentially by atmospheric plasma spraying to medical implant surfaces are a mainstay of modern implantology. During contact with the hot plasma jet, HAp particles melt incongruently and undergo complex dehydration and decomposition reactions that alter their phase composition and crystallographic symmetry, and thus, the physical and biological properties of the coatings. Surface analytical methods such as laser-Raman and nuclear magnetic resonance (NMR) spectroscopies are useful tools to assess the structural changes of HAp imposed by heat treatment during their flight along the hot plasma jet. In this contribution, the controversial information is highlighted on the existence or non-existence of oxyapatite, i.e., fully dehydrated HAp as a thermodynamically stable compound.

Keywords: hydroxylapatite; oxyhydroxylapatite; oxyapatite; tricalcium phosphate; tetracalcium phosphate; Raman spectroscopy; MAS-CP NMR spectroscopy; 2D-HETCOR NMR spectroscopy

Citation: Heimann, R.B. Structural Changes of Hydroxylapatite during Plasma Spraying: Raman and NMR Spectroscopy Results. *Coatings* **2021**, *11*, 987. https://doi.org/10.3390/coatings11080987

Academic Editor: Angela De Bonis

Received: 23 July 2021
Accepted: 15 August 2021
Published: 19 August 2021

1. Introduction

Among various bioactive calcium orthophosphates utilized in medical devices, hydroxylapatite (HAp) takes on particular important roles. Applications are ranging from coatings for hip and knee endoprostheses, to densified monolithic implants for dental root replacement, to bone cavity filler, to three-dimensional bone repair scaffolds, and to advanced hybrid hydroxylapatite-polymer nanocomposites with enhanced osseoconductive, angiogenic, and antimicrobial functions able to mimic salient biological properties. All this is based on the chemical and structural similarity of hydroxylapatite to the inorganic constituent of bone and teeth. Although non-stoichiometric biological apatite differs from stoichiometric geological apatite in terms of crystalline order, crystallite size, defect density, amount of hydroxyl anions, as well as degree of cationic and anionic substitution, synthesized hydroxylapatite serves well as a proxy for its natural counterpart. Osseoconductive hydroxylapatite coatings are being predominantly deposited on implant materials by atmospheric plasma spraying despite the fact that its crystallographic structure and phase composition suffers from exposure to the high temperature plasma jet. Hence, to achieve optimum biomedical performance of plasma-sprayed hydroxylapatite coatings in contact with living tissue, their structural alteration in the hot plasma jet must be carefully assessed and considered when designing coating systems for medical application.

Since hydroxylapatite coatings on medical implants will be in contact with extracellular fluid (ECF), their performance and structural changes were studied copiously in the past by Raman [1–6], nuclear magnetic resonance (NMR) [7–11], and X-ray photoelectron spectroscopies (XPS) [12]. Stammeier et al. [6] investigated the kinetics of the amorphous calcium phosphate (ACP) to crystalline HAp transformation at ambient temperature and pH = 9.2 by taking highly time-resolved in-situ Raman spectroscopy spectra at a rate of 100 spectra/h. Their results showed that after 18 h, transformation of ACP to crystalline HAp occurred as demonstrate in a peak shift from 950 to 960 cm^{-1} as well as in a sharpening of the 960 cm^{-1} peak. Likewise, solid-state NMR work by Jäger et al. [11] revealed that HAp nanoparticles possess a crystalline core with Ca/P = 1.67 akin to stoichiometric HAp

but are covered by an approximately 1 nm thin disordered surface film with Ca/P~1.5 dominated by HPO_4^{2-} anions and structural water. This leads to the conclusion that the surface of n-HAp is critically different from bulk HAp, with important consequences for the ability to bind protein molecules essential for osseointegration. Solid-state NMR in conjunction with ab initio modelling has been found capable of fully describing the surface structure and chemistry of HAp, essential to understand its reactivity towards the organic matrix of bone [10].

The present contribution describes results of Raman and NMR spectroscopic investigations applied to assess the stepwise dehydration and decomposition reactions of hydroxylapatite subjected to plasma spraying. Such information provides important clues to predict the biomedical performance of HAp coatings, deposited on medical implants, in contact with living tissue.

2. Structure of Hydroxylapatite

Hydroxylapatite, $Ca_{10}(PO_4)_6(OH)_2$ is a member of a large group of chemically different but crystallographically identical compounds with the general formula $M_{10}(ZO_4)_6X_2$. Today, some sixty members with this structure are known as natural minerals as well as synthetic compounds. Large M cations are Ca, Sr, K, Na, Cd, Pb, Zn, La, Ce, and several others; small tetrahedrally coordinated Z cations entering the structure may be P, V, As, Cr, Si, C, Al, and S, whereas X are OH, Cl, F, CO_3, and H_2O, as well as vacancies □ that are located in the wide channels parallel to [00.1]. Hydroxylapatite crystallizes in the hexagonal space group $P6_3/m$ (S.G. 176). Figure 1A shows Ca_IO_9 polyhedra chains (grey) parallel to [00.1] with 6_3 screw characteristic. The chains share corners and edges with $[PO_4]$ tetrahedra (green) to yield a hexagonal array. Figure 1B depicts details of the ion environment around the *c*-axis. Two oxygen ions of the $[PO_4]$ tetrahedra are found above and below mirror planes through $z = ¼$ and $z = ¾$. The non-equivalent Ca^{2+} ions are located at two different positions: Ca_I at z = 0 and z = ½ along the three-fold axes a_i (Wyckoff position 4*f*), and Ca_{II} at $z = ¼$ and $z = ¾$ along the hexagonal screw axis 6_3 parallel [00.1] (Wyckoff position 6*h*). Hence, considering the two non-equivalent Ca positions, a more accurate formula of hydroxylapatite is $[(Ca_I)_4(Ca_{II})_6](PO_4)_6(OH)_2$. The X anions are located at $z = ¼$ and $z = ¾$. Their exact positions depend on their size: the smaller F^- anion in fluorapatite is positioned exactly at the center of the triangles formed by the three Ca_{II} cations, the larger OH^- anion in hydroxylapatite is off-center by an increment δ = 0.36 Å [13] (Figure 1B).

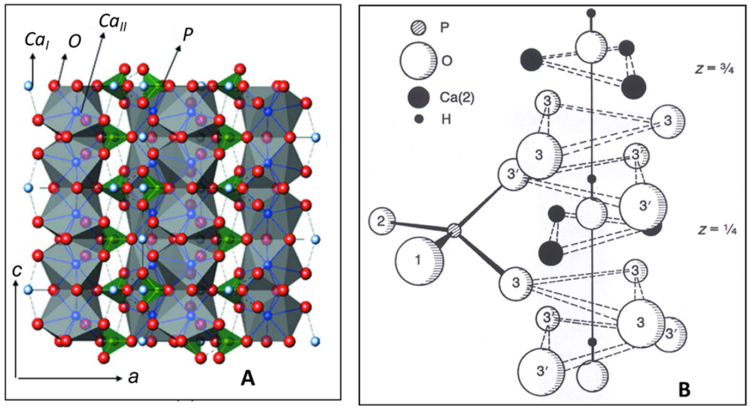

Figure 1. (**A**): Crystallographic structure of HAp with a hexagonal unit cell a = 0.9432 nm, c = 0.6881 nm [14]. Blue spheres: Ca^{2+}; green spheres: P^{5+}; red spheres: O^{2-}. Ca_IO_9 polyhedra chains parallel to [00.1] are linked by $[PO_4]$ coordination tetrahedra. © Reproduced with permission of the International Union of Crystallography. (**B**): Details of the arrangement of the Ca_{II} ions at $z = ¼$ and ¾, and O^{2-} ions surrounding the 6_3 screw axis parallel to [00.1]. The OH^- anions are positioned within the triangular Ca_{II} configuration at $z = ¼ + δ$ and $z = ¾ + δ$ [15]. © Reprinted with permission from Elliott et al., Adv. X-ray Anal. 45, 172–181 (2002). Copyright 2002, JCPDS-International Centre for Diffraction Data.

3. Thermal Alteration during Plasma Spraying

Thermal exposure during their flight along the plasma jet renders HAp particles to melt incongruently, i.e., they do not melt uniformly by retaining their stoichiometric composition, but react and decompose to form two solids of different composition plus liquid. This is shown in the inset of the CaO-P_2O_5 phase diagram where at 1570 °C hydroxylapatite decomposes to form α-$Ca_3(PO_4)_2$, $Ca_4O(PO_4)_2$, and melt (Figure 2).

Prolonged heating causes the calcium phosphate-containing liquid to lose volatile P_2O_5, thus shifting its composition along the liquidus line towards CaO-richer compositions. This process is accelerated by reduction reaction with hydrogen that is frequently added to the plasma-forming gases to increase the plasma enthalpy and, in turn, the heat transfer rate from the thermal plasma to the HAp powder particles flying along the center line of the plasma jet [16].

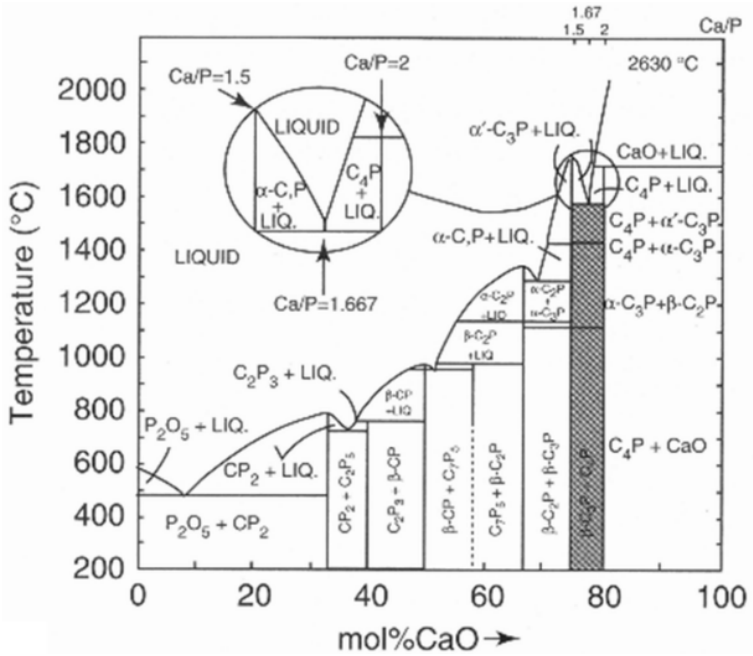

Figure 2. Phase diagram of the water-free binary system CaO-P_2O_5 showing the incongruent melting of hydroxylapatite with Ca/P = 1.667 (inset) [17]. The compositions are given in cement chemical notation, i.e., C = CaO, P = P_2O_5. © Reprinted with permission from E.R. Kreidler and F.A. Hummel, Inorg. Chem., 1967, 6(5), 884–891. Copyright 1967 Am. Chem. Soc.

The stepwise thermal decomposition of HAp starts with a dehydration reaction that produces disordered oxyhydroxylapatite (OHAp) and eventually oxyapatite (OAp) according to Equations (1) and (2).

$$Ca_{10}(PO_4)_6(OH)_2 \rightarrow Ca_{10}(PO_4)_6(OH)_{2-2x}O_x\square_x + xH_2O, \quad (1)$$

$$Ca_{10}(PO_4)_6(OH)_{2-2x}O_x\square_x \rightarrow Ca_{10}(PO_4)_6O_x\square_x + (1-x)H_2O, \quad (2)$$

During thermal exposure, partially dehydrated hydroxylapatite (oxyhydroxylapatite, OHAp) was found to alter its crystallographic symmetry from the archetypical $P6_3/m$ to a triclinic $P\bar{1}$ space group when the amount of structurally bound hydroxyl groups is removed in excess of about 35% [18]. The reason for this triclinic distortion has been tentatively attributed to tilting of the hydroxyl ions located in the c-channels away from the channel axis. There are earlier statements that HAp retains its $P6_3/m$ space group up to a hydroxyl loss of 75%. Indeed, Liao et al. [19] reported that even a loss of chemically bound water as high as 75% retains the channel structure of apatite. The limiting composition is then $Ca_{10}(PO_4)_6(OH)_{0..5}O_{0.75}\square_{0.75}$ that corresponds

to a water loss of 1.34% [20]. According to Alberius-Henning et al. [18], the degree of dehydration of 78% marks the onset of decomposition of the apatite structure. At this point, the unit cell parameters of OHAp with triclinic $P\bar{1}$ symmetry were determined to be a = 0.940023(3) nm, b = 0.939704(3) nm, c = 0.689967(72) nm, α = 90.0626(2)°, ß = 89.7478(1)°, and γ = 119.9971(2)°, very close to a hexagonal metric (Table 1). OHAp has been described formally either as a non-stoichiometric defect HAp [21,22] or a 1:1 solid solution of stoichiometric HAp and OAp [23].

Even more mysteries surround the oxyapatite structure. Oxyapatite, $Ca_{10}O(PO_4)_6$, the product of complete dehydration of hydroxylapatite [24], was first proposed by the British chemist John A. Voelcker [25], and subsequently identified as a natural mineral and named voelckerite in his honor by the American mineralogist Austin F. Rogers [26]. However, this elusive mineral was later correctly described as fluorapatite. Oxyapatite is known to convert back to HAp during cooling of the as-sprayed coating in the presence of moist air or by reacting with extracellular fluid (ECF) in vivo. This reaction is governed by the equation $O^{2-}(s) + \square(s) + H_2O(g) \rightarrow 2OH^-$ (s).

Although in the past the existence of oxyapatite as a thermodynamically stable compound has been questioned [27–29], some evidence to the contrary exists [20,30]. Trombe and Montel showed that OAp is only stable under vacuum or in water-free inert gases between 850 and 1050 °C, but decomposes beyond 1050 °C into tri- and tetracalcium phosphates [30]. Modelling using density-functional theory with local-density approximation (DFT-LDA) for considering the exchange and correlation parts of the electron interactions, and first-principles pseudopotentials for the electron-ion interactions has postulated a hexagonal defective 'c-empty' structure $Ca_{10}(PO_4)_6\square_2$ with a stable total energy minimum and an c_0 value of 0.682 nm [31]. Earlier studies have assumed in the structure of OAp a linear chain of O^{2-} ions parallel to [00.1], each one followed by a vacancy, conforming to a reduced space group of $P\bar{6}$ by loss of the mirror plane m as shown in Figure 3B [32].

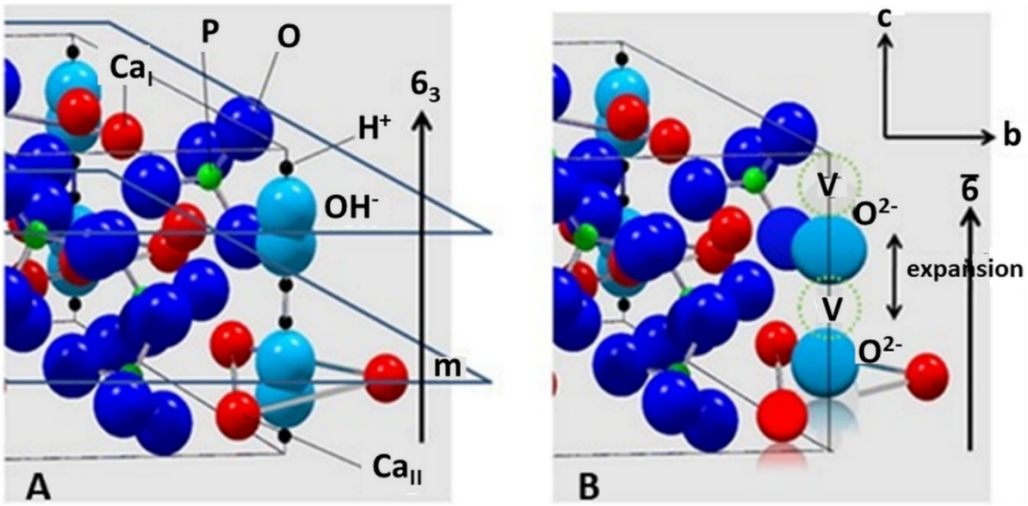

Figure 3. (**A**): Ball-and-spoke model of hydroxylapatite with space group $P6_3/m$. There are mirror planes m through z = ¼ and z = ¾, perpendicular to the c-axis with 6_3 characteristics. The non-equivalent Ca_I and Ca_{II} positions are indicated. (**B**): Hypothetical structure of oxyapatite, S.G. $P\bar{6}$. There is a chain of O^{2-} ions separated by vacancies V along the polar hexagonal axis $\bar{6}$. © Reprinted with permission from R.B. Heimann, Materialwiss. Werkstofftechn., 2009, 40(1–2), 23–30. Copyright 2009 Wiley.

Although the space group $P\overline{6}$ suggested by Alberius-Henning et al. [32] could be confirmed by the calculations of Calderin et al. [31], the c_0 value found by the former authors was only 0.673 nm, substantially shorter than that calculated by Calderin et al. and even shorter than the experimental value of 0.6930(8) nm obtained by Gross et al. [33] using synchrotron radiation (Table 1). Moreover, it was suggested by De Leeuw et al. that the formation of water or oxygen defects and a pile-up of oxygen vacancies in the c-channels (Figure 3B) is thermodynamically unfavorable [28]. In conclusion, the jury is still out whether oxyapatite could be considered a thermodynamically stable compound in the CaO-P_2O_5 phase diagram.

Unequivocal detection of OAp by conventional X-ray diffraction is difficult [34,35] since its *c*-axis dimension is only marginally larger than that of HAp [35–37]. This results in only a small shift of the (00.2) interplanar spacing towards smaller diffraction angles. Consequently, very accurate measurements are needed as provided by single crystal diffraction using high-resolution synchrotron radiation or neutron diffraction. The lattice expansion during dehydration shown in Figure 3B is likely effected by the larger Shannon crystal radius of the O^{2-} ion (135 pm) compared to that of the OH^{-} ion (118 pm).

Additional investigation by the present author using synchrotron radiation [38] showed that atmospheric plasma spraying of stoichiometric HAp with comparatively low plasma power (11 kW) results in reversible dehydration, yielding OAp with c_0 = 0.6902(3) nm, somewhat longer compared to the value of c = 0. 6881 nm found for stoichiometric HAp. Figure 4A shows the synchrotron radiation diffraction pattern of plasma-sprayed HAp powder with mean grain size around 120 µm. The only crystalline phases detectable are OAp (Powder Diffraction File 04-011-1880 and 89-649) and ß-TCP (Powder Diffraction File 9-016978). However, the strongly elevated background between about 25 and 35 °2θ with a centroid of 31 °2θ suggests the presence of sizeable amounts of amorphous calcium phosphate (ACP). Quantitative estimation of the ACP content by the Keller and Dollase method [39] revealed ACP contributions of 25% (low plasma power: 11 kW) and 40% (high plasma power: 24 kW), respectively. Figure 4B shows the synchrotron diffraction pattern of the (00.2) and (00.4) interplanar spacings of HAp and OAp. Values of the scattering vectors Q of the (00.2) and (00.4) interplanar spacings obtained from the Powder Diffraction File are given for comparison, showing that the Q vectors measured are between those of HAp (PDF 9-432) and OAp (PDF 89-649). From the measured Q-values of 1.821 $Å^{-1}$ and 3.640 $Å^{-1}$, the c_0-values of OAp were calculated to be 0.6900(0) nm and 0.6904(6) nm, respectively, approximately 0.3% longer than that of HAp with 0.6881(4) nm. This confirms earlier data by Montel et al. [37].

During continuing exposure to high temperatures, OAp decomposes further to tricalcium phosphate (α-TCP) and tetracalcium phosphate (TTCP) [30] according to

$$Ca_{10}(PO_4)_6O_x\square_x \rightarrow 2\ \alpha\text{-}Ca_3(PO_4)_2 + Ca_4O(PO_4)_2. \quad (3)$$

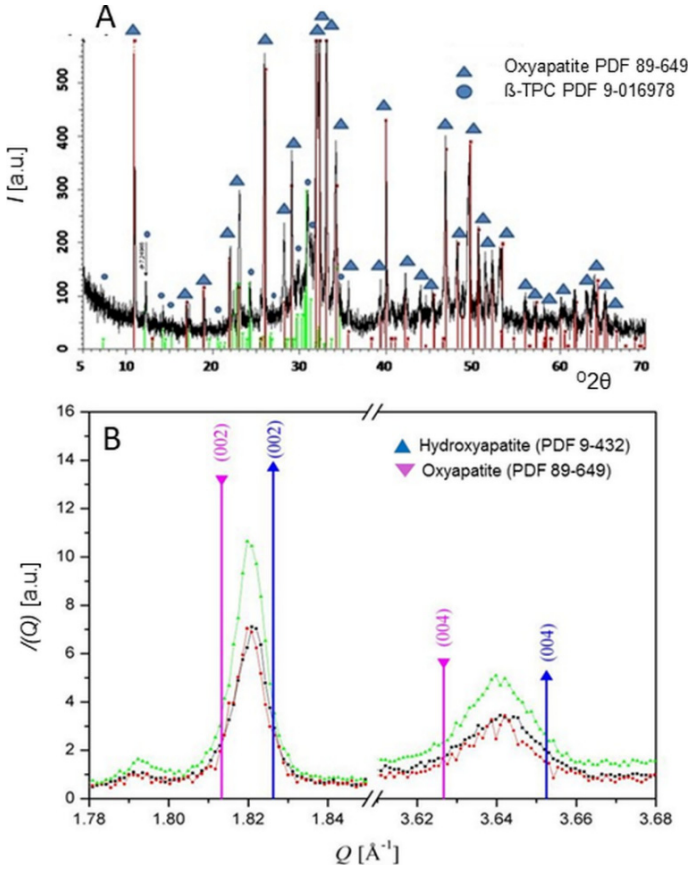

Figure 4. (**A**): High-resolution synchrotron radiation diffraction pattern of HAp coatings, deposited with low plasma power of 11 kW, show mainly oxyapatite with minor contribution of ß-tricalcium phosphate [38]. Additional plasma spray parameters were selected as follows: plasma gas (argon) flow rate 50 slpm, powder feed rate 18 g/min, spray distance 100 mm, and translation speed 30 m/min. (**B**): Scattering vectors Q (= $4\pi \times \sin\theta/\lambda$) of the diffraction profiles of three plasma-sprayed HAp coatings around (00.2) and (00.4) interplanar spacings of HAp (blue) and OAp (pink). Synchrotron radiation obtained from Angströmquelle Karlsruhe GmbH (ANKA), λ = 0.95 Å; step size 0.05 °2θ; range 2.0–52 °2θ. © Reprinted with permission from R.B. Heimann, Materialwiss. Werkstofftechn., 2009, 40(1–2), 23–30. Copyright 2009 Wiley.

Tetracalcium phosphate is the least stable calcium orthophosphate and crystallizes in the monoclinic space group $P2_1$. In its structure, the Ca^{2+} and $[PO_4]^{3-}$ ions are positioned in four sheets that are perpendicular to the *b*-axis. Each sheet contains two Ca^{2+}-$[PO_4]^{3-}$ columns and one Ca^{2+}-Ca^{2+} column, yielding an structural arrangement similar to glaserite, $K_3Na(SO_4)_2$. Two neighboring sheets constitute a structure closely related to the HAp structure [40].

At high plasma enthalpies, both α-TCP and TTCP further decompose, forming cytotoxic CaO according to

$$Ca_3(PO_4)_2 \rightarrow 3CaO + P_2O_5, \quad (4)$$

or

$$Ca_4O(PO_4)_2 \rightarrow 4CaO + P_2O_5. \quad (5)$$

Table 1 summarizes the space groups and unit cell parameters of HAp and its dehydration and decomposition phases considered in this contribution.

Table 1. Crystallographic data of dehydration and decomposition products of hydroxylapatite. S.G. space group, HAp hydroxylapatite, m-HAp monoclinic hydroxylapatite, OHAp oxyhydroxylapatite, OAp oxyapatite, TTCP tetracalcium phosphate, TCP tricalcium phosphate. n.d. = not determined, * calculated crystallographical structures.

Phase	S.G.	a_0 (nm)	b_0 (nm)	c_0 (nm)	α (°)	ß (°)	γ (°)	Reference
HAp	$P6_3/m$	0.9432	0.9432	0.6881			120	[41]
HAp	$P6_3/m$	0.9418	0.9418	0.68827			120	[42]
c-empty *	$P6_3/m$	0.910	0.910	0.682			120.1	[31]
m-HAp	$P2_1/b$	0.9421	$2a_0$	0.6881			120	[43]
OHAp	$P\bar{1}$	0.9400	0.9397	0.6899	90.063	89.748	119.997	[18]
OAp	$P\bar{6}$	0.9432	0.9432	0.6881			120	[32]
OAp	$P\bar{6}$	n.d.	n.d.	0.6902			n.d.	[38]
OAp	$P\bar{6}$	n.d.	n.d.	0.6931			n.d.	[43]
OAp *	$P\bar{6}$	0.906	0.906	0.673	90.03	90.00	119.9	[31]
TTCP	$P2_1$	0.7023	1.1986	0.9473		90.901		[40]
α-TCP	$P2_1/a$	1.2873	2.7280	1.5213		126.208		[44]
ß-TCP	$R3c$	1.0435	1.0435	3.7403			120	[45]

4. Raman Spectroscopy

The thermal alteration reactions of HAp described above can be traced by surface analytical techniques, for example, by Fourier-transform infrared spectroscopy (FTIR) or µ-laser-Raman spectroscopy (LRS) [46]. Figure 5A depicts the four principal Raman modes ν_1 to ν_4 of the [PO_4] tetrahedron. The ν_1 band is the high-intensity symmetric stretching mode of the P–O bond (point symmetry A_1(R)), and the ν_2 is the result of the doubly degenerate O–P–O bending mode (point symmetry E(R)). Lower intensity vibrational modes are ν_3 related to the triply degenerate asymmetric O–P–O stretching mode (point symmetry F_2(I,R)), and ν_4 related to the triply degenerate O–P–O bending mode, also with point symmetry F_2(I,R). Figure 5B shows details of the Gaussian–Lorentzian deconvolution of the principal ν_1 mode at 962 cm^{-1} as the main contribution typical for well-ordered stoichiometric HAp, and minor contributions at 971 cm^{-1} assigned to ß-TCP and 949 cm^{-1} likely related to ACP.

Demnati et al. [47] reported the results of Gaussian–Lorentzian deconvolution of the $\nu_1(PO_4)$ Raman stretching domain of a plasma-sprayed HAp coating deposited with low plasma energy. They showed that the low intensity contribution of ACP around 950 cm^{-1} was masked by a strong signal of OAp. In addition, a second Raman band between 966 and 969 cm^{-1} was assigned to OAp. Hence, curve fitting revealed that OAp may be characterized by two Raman bands at 950.43 ± 0.02 and 969.93 ± 0.01 cm^{-1}. However, the first vibration band might also be assigned to ACP [6] and the second one to ß-TCP as indicated in Figure 5B. Hence, more sophisticated high-resolution surface analytical methods must be employed to confirm or refute the stable existence of OAp outside the experimental restrictions stipulated by Trombe and Montel [30].

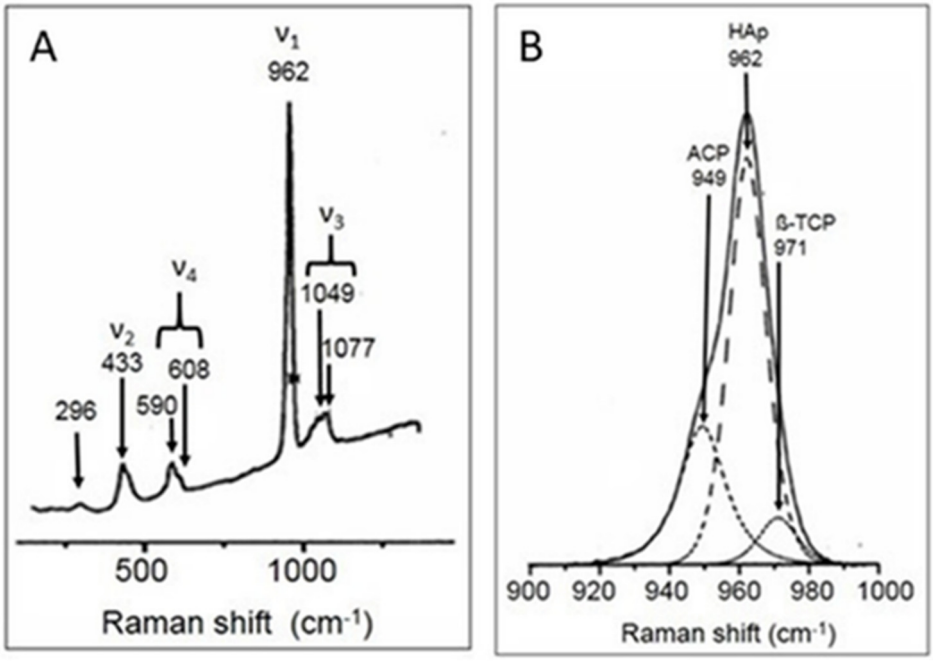

Figure 5. (**A**): Principal Raman vibrational modes of the [PO_4] tetrahedron of plasma-sprayed HAp. (**B**): Gaussian–Lorentzian deconvolution of the ν_1 mode (Ar+ laser wavelength λ = 514.6 nm; beam diameter 3 µm; laser power 5 mW) [38,48,49]. Raman microprobe T 64000 (Jobin Yvon), Dept. of Theoretical Physics, TU Bergakademie Freiberg, Germany. © Reprinted with permission from R.B. Heimann, Materialwiss. Werkstofftechn., 2009, 40(1–2), 21–30. Copyright 2009 Wiley.

5. Nuclear Magnetic Resonance Spectroscopy

Even under the tenuous assumption that the general crystallographic symmetry of HAp is maintained during plasma spraying at low plasma enthalpies, substantial changes may be induced related to the spatial arrangement of ions, and thus, deviations from their equilibrium positions. In particular, the Ca_I ions are shifted from their equilibrium positions at $z = 0$ and $z = ½$, the [PO_4] tetrahedra are distorted with a Baur distortion coefficient of D_1(TO) of ~0.3, the Ca_I-Ca_I distances are shortened with associated changes of the Ca–O distances, and the sub-structural $[Ca_5(PO_4)_3]^+$ clusters are flattened along the *c*-axis. In addition, the Ca_I-O_{II} distances increase from 0.246 to 0.257 nm, and the Ca_I-O_I distances decrease from 0.240 to 0.230 nm [50]. These distortions have important consequences for the thermal stability and dissolution behavior of plasma-sprayed HAp coatings.

5.1. MAS-CP NMR Spectra

To assess the lattice distortion and thus, the degree of disorder imposed by plasma spraying, NMR is being used, an analytical technique able to reveal differently distorted [PO_4] tetrahedra and their association with [OH] groups [21,22,51–53]. NMR spectroscopy can be carried out in magic angle spinning (MAS) and cross-polarization (CP) modes. The positions and shift of ^{1}H-MAS and ^{31}P-MAS NMP bands are utilized to deduce the environment of the [PO_4] tetrahedra, and thus, allow to distinguish among short range-ordered (SRO) dehydration phases such as OHAp/OAp and thermal decomposition phases such as TCP and TTCP.

Figure 6A,B show ^{1}H-MAS and ^{31}P-MAS NMP spectra of as-sprayed hydroxylapatite coatings [22]. Whereas highly crystalline, stoichiometric HAp is characterized by a single proton position at -0.1 ± 0.1 ppm (Figure 6A, inset, band *L*), HAp exposed to the high-temperature plasma jet shows additional band positions at -1.3 ± 0.3 ppm (band *L**) as well as 5.2 ± 0.3 ppm (band M), whereby the isotropically shifted band *L** is associated with protons in distorted short range-ordered (SRO) structures of thermally stressed HAp,

and band M is attributed to isolated pairs of strongly coupled protons in the channels parallel the *c*-axis [52]. The band G at 1.3 ppm belongs to mobile free water molecules.

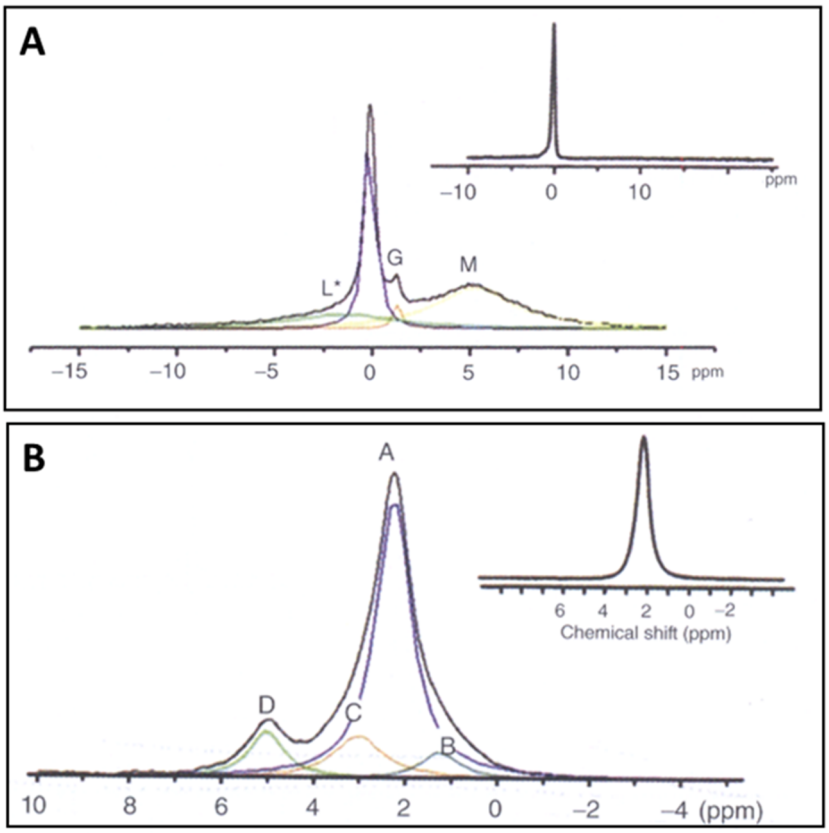

Figure 6. (**A**): ^{1}H-MAS NMR spectrum of as-sprayed HAp. For band assignment see text. (**B**): ^{31}P-MAS NMR spectrum of as-sprayed HAp [52,53]. For band assignment see text. The insets show spectra of highly ordered, stoichiometric hydroxylapatite [21]. Bruker AMX 400 (rotation rate 12.5 kHz, pulse length 2 µs, repetition rate 200 s). Dept. of Optic and Quantum Electronics, University of Jena, Germany © Reprinted with permission from R.B. Heimann and H.D. Lehmann, Biomedical Coatings for Medical Implants (Wiley-VCH, Weinheim, 2015). Copyright 2015 Wiley-VCH.

The assignment of NMR signals in the ^{31}P-MAS spectrum is more complex. The inset of Figure 6B shows the single band A of a completely ordered, highly crystalline HAp at 2.3 ± 0.1 ppm [21]. Thermal exposure by plasma spraying adds several additional bands to the deconvolved NMR spectrum at 5.0 ± 0.2 ppm (band D), 3.0 ± 0.2 ppm (band C), and 1.5 ± 0.2 ppm (band B) that have been attributed [21,22] as follows: band D may belong to very strongly distorted [PO_4] groups without associated [OH], band C to distorted [PO_4] tetrahedra with single or paired [OH] groups, and band B to strongly distorted [PO_4] groups without nearby [OH]. These features have been tentatively related to TCP + TTCP (band D), OHAp (band C), and OAp (band B) [21,22] but may be open to other interpretation. For example, although the ^{31}P-MAS-NMR spectrum of Figure 6B shows a noticeable D band, this band is missing in the HETCOR spectrum (Figure 7A), i.e., is not correlated to protons. This may suggest that the D band is indicative of [PO_4] tetrahedra existing in a proton-depleted region of the apatite channel structure and thus, may belong to OAp [53]. Moreover, in the ^{31}P spectrum, the D band has been assigned to the typical NMR band of TTCP under the reasonable assumption that with progressing loss of OH^- ions the nature of the decomposition product of HAp approaches the structure of TTCP, along the dehydration/decomposition reaction chain HAp→OHAp→OAp→TTCP (+TCP) as shown in Equations (1)–(3) and also expressed by the evolutionary structural sequence $P6_3/m \rightarrow P\bar{1} \rightarrow P\bar{6} \rightarrow P2_1$ (see Table 1).

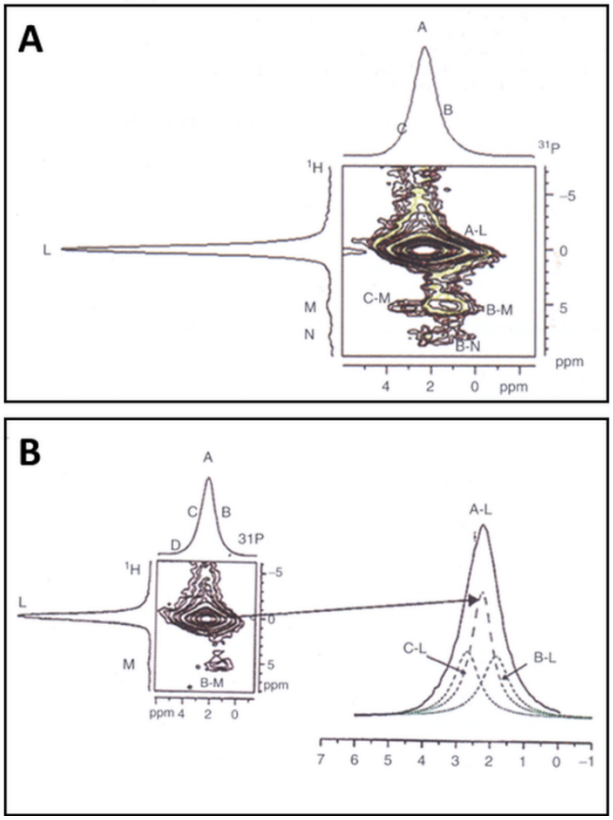

Figure 7. (**A**): 2D-^{1}H/^{31}P-CP-HETCOR NMR spectrum of a plasma-sprayed HAp coating [53,54]. Band assignments according to Ref. [21]. (**B**): 2D-^{1}H/^{31}P-CP-HETCOR NMR spectrum of a plasma-sprayed HAp coating incubated for 12 weeks in simulated body fluid [55]. The cross-section of the HETCOR spectrum at the proton frequency of band L shows reduction and disappearance, respectively, of the HETCOR signals C-M, B-M, and B-N [54]. © Reprinted with permission from R.B. Heimann and H.D. Lehmann, Biomedical Coatings for Medical Implants (Wiley-VCH, Weinheim, 2015). Copyright 2015 Wiley.

5.2. Heteronuclear Correlation (HETCOR) NMR Spectra

The 2D-double quantum ^{1}H/^{31}P cross-polarization heteronuclear correlation (HETCOR) NMR spectra shown in Figure 7A,B are dominated by a cross-sectional A–L band, typical for well-crystallized and close to-stoichiometric HAp. In addition, minor contributions of C–M (strongly distorted [PO_4] tetrahedra with paired [OH]) and B–M (distorted [PO_4] tetrahedra with isolated paired [OH]) can be assigned to OHAp and Ca-deficient ACP, respectively. The weak M and N bands in the ^{1}H spectrum around 5 ppm and 7.5 ppm, respectively, can be associated with isolated pairs of strongly coupled protons and isolated [OH] groups in the HAp channels, signaling an advanced dehydration state. These NMR results suggest that the investigated plasma-sprayed HAp coatings contain only more or less stoichiometric HAp, partially dehydroxylated HAp (OHAp). Minor contributions of TCP and TTCP are also present, as results of thermal decomposition of OAp as shown in Equation (3).

The origin of the distortion of structural elements of HAp as described above [50] is related to internal residual microscopic stresses. These stresses are the result of the massive temperature gradient that is manifest when hot molten particles impinge on the comparatively cool substrate surface. The hot particles will be instantaneously quenched with cooling rates of 10^{6}–10^{7} K/s. Since the contraction of the solidified particles is constrained by their adherence to the micro- or nano-roughened substrate surface, strong tensile and/or compressive surface stresses occur. These stresses are, at least in part, responsible for the distortion of the crystallographic symmetry of the HAp particles splats.

Prolonged contact of as-sprayed HAp coatings in vitro with simulated body fluid (SBF) [55] or extracellular fluid (ECF) in vivo results in dissolution of easily soluble calcium phosphate phases. Comparison of Figure 7A,B shows that most of the thermal decomposition phases have disappeared and consequently, the amount of near-stoichiometric HAp has substantially increased. However, it is remarkable that disordered HAp structures and TCP as well as TTCP remain in the coatings even after incubation for as long as 12 weeks. This is presumably the result of the dense nature of the coating that prevents SFB from penetrating deeply into the coating body. Approximate quantification shows that the amount of HAp strongly increased from about 50 mass% in as-sprayed coatings to 75 mass% after 12 weeks immersion in r-SBF. Concurrently, the amount of disordered HAp phases (OHAp/OAp) decreased from 36 mass% to only 16 mass%, and the amount of TCP+TTCP remained roughly constant around 20 mass% [56]. The latter finding contrasts with results obtained by Otsuka et al. [54] that TTCP dissolved much faster than ß-TCP when immersed in SBF [57].

6. Biomedical Relevance

Today, hydroxylapatite-based coatings are copiously applied to implant surfaces to elicit osseoconductive and, in the presence of adsorbed cytokines and non-collagenous proteins, osseoinductive properties [58]. These coatings are being deposited predominantly by atmospheric plasma spraying (APS) [16], a technology that provides an economically and biomedically viable choice to functionalize metallic implant surface destined to be in prolonged contact with living tissue. At present, deposition by APS of HAp onto the stems of hip endoprostheses [59] or roots of endosseous dental implants [60] is the only method approved by US-FDA to coat implant surfaces for clinical use [61]. There exists a long list of contributions describing in many details the deposition technique, physicochemical properties, and clinical performance of HAp coatings [62]. Stringent property and performance requirements are codified by standard specifications [63–65].

Thermal dehydration and decomposition of plasma-sprayed HAp affect and control the properties and the characteristics of bioceramic coatings. The fact that the OH^- positions of HAp can be occupied by mobile O^{2-} ions or by vacancies is of vital importance for understanding the kinetics of the dehydration reaction of HAp towards OHAp and eventually OAp when subjected to high temperature during plasma spraying. Whereas the occurrence and structural behavior of OH^- ions in the HAp lattice has been recognized and widely studied in synthetic material, natural biological bone-like apatite was found to be essentially free of OH^- ions when looking at Raman spectroscopy data [66,67]. Subsequently, this surprising finding was confirmed by NMR spectroscopy and inelastic neutron scattering. Hence, contrary to the general medical nomenclature, bone-like apatite appears to be non-hydroxylated. However, there has been found a strong correlation between the concentration of OH^- ions and the crystallographic degree of atomic order. While it is not obvious how charge balance can be maintained within an essentially OH^--free nanocrystalline apatite lattice, there are now suggestions [66,67] that the specific state of atomic disorder, imposed biochemically by the body, is an essential precondition of cell metabolism. In addition, there are assumptions that the lack of hydroxyl ions in the lattice of nanocrystalline biological Ca-deficient HAp causes a high density of vacancies along the *c*-axis (Figure 3B) and hence, a high mobility of Schottky-type defects that in turn, influence its solubility and provide a mechanism for fast and efficient bone reorganization by dissolution (osteoclastesis) and reprecipitation (osteoblastesis) during bone reconstruction in response to changing stress and load levels according to Wolff's law [68].

7. Conclusions

HAp coatings for medical application [62] are in need of carefully designed and optimized deposition conditions, achieved by closely controlling key properties such as chemical and phase composition and degree of crystallinity. In addition, other intrinsic

coating properties must be optimized including coating thickness, adhesion and cohesion strength, porosity and pore size distribution, surface nanostructure and degree of fractality, sign and strength of residual coating stresses, crystallographic orientation, and finally, favorable dissolution kinetics during contact with extracellular fluid (ECF) when implanted in the human body [62,69,70]. High-resolution surface analytical techniques such as Raman and NMR spectroscopies are important tools to investigate and control composition and structural state of HAp coatings designed to perform well as osseoconductive coatings for a variety of medical implants.

Despite much progress related to the biomedical performance of plasma-sprayed biomedical coatings based on hydroxylapatite, there is an urgent need for improvement. Improvements may pertain to replacement of Ca^{2+} cations by metabolically important elements such as Sr, Mg, K, Na, Zn, and others known to be present in biological apatite, replacement of PO_4^{3-} anions by CO_3^{2-}, SiO_4^{4-}, or SO_4^{2-} as well as replacement of OH^- anions by Cl^-, F^-, O^{2-}, and CO_3^{2-}. Such replacement even in small concentration affects many biochemical pathways in which bone matter is involved [58,69]. Finally, tailoring the microstructure of plasma-sprayed hydroxylapatite surfaces by laser ablation, chemical etching or mechanical roughening will lead to enhanced adhesion of bone growth-supporting proteins and thus, promote adhesion, proliferation, vitality, and spreading of bone cells [71].

Funding: This research received no external funding.

Institutional Review Board Statement: Not applicable.

Informed Consent Statement: Not applicable.

Data Availability Statement: No new data were created or analyzed in this study. Data sharing is not applicable to this article.

Conflicts of Interest: The author declares no conflict of interest.

References

1. Silva, C.C.; Sombra, S. Raman spectroscopy measurements of hydroxyapatite obtained by mechanical alloying. *J. Phys. Chem. Sol.* **2004**, *65*, 1031–1033. [CrossRef]
2. Ulian, G.; Valdrè, G.; Como, M.; Ugliengo, P. The vibrational features of hydroxylapatite and type A carbonated apatite: A first principle contribution. *Am. Mineral.* **2013**, *98*, 752–759. [CrossRef]
3. Nosenko, V.V.; Yaremko, A.M.; Dzhagan, V.M.; Vorona, I.P.; Romanyuk, Y.A.; Zatovsky, I.V. Nature of some features in Raman spectra of hydroxyapatite-containing materials. *J. Raman Spectrosc.* **2016**, *47*, 726–730. [CrossRef]
4. Antonakos, A.; Liarokapis, E.; Kyriacou, A.; Leventouri, T. Raman and IR studies of the effect of Fe substitution in hydroxyapatite and deuterated hydroxyapatite. *Am. Mineral.* **2017**, *102*, 85–91. [CrossRef]
5. Mohonta, S.K.; Maria, K.H.; Rahman, S.; Das, H.; Hoque, S.M. Synthesis of hydroxyapatite nanoparticles and role of its site in hydroxyapatite/chitosan-gelatin biocomposite for bone grafting. *Int. Nano Lett.* **2021**. [CrossRef]
6. Stammeier, J.A.; Purgstaller, B.; Hippler, D.; Mavromatis, V.; Dietzel, M. In-Situ Raman spectroscopy of amorphous calcium phosphate to crystalline hydroxyapatite transformation. *MethodsX* **2018**, *5*, 1241–1250. [CrossRef]
7. Rothwell, W.P.; Waugh, J.S.; Yesinowski, J.P. High-resolution variable-temperature ^{31}P NMR of solid calcium phosphates. *J. Am. Chem. Soc.* **1980**, *102*, 2637–2643. [CrossRef]
8. Yesinowski, J.P.; Wolfgang, R.A.; Mobley, M.J. New NMR methods for the study of hydroxyapatite surfaces. In *Adsorption on and Surface Chemistry of Hydroxyapatite*; Misra, D.N., Ed.; Springer: Boston, MA, USA, 1984; pp. 151–175.
9. Mason, H.E.; Kozlowski, A.; Phillips, B.L. Solid-state NMR study of the role of H and Na in AB-type carbonate hydroxylapatite. *Chem. Mater.* **2007**, *20*, 294–302. [CrossRef]
10. Chappell, H.; Duer, M.; Groom, N.; Pickard, C.; Bristowe, P. Probing the surface structure of hydroxyapatite using NMR spectroscopy and first principles calculations. *Phys. Chem. Chem. Phys.* **2008**, *10*, 600–606. [CrossRef]
11. Jäger, C.; Welzel, T.; Meyer-Zaika, W.; Epple, M. A solid-state NMR investigation of the structure of nanocrystalline hydroxyapatite. *Magn. Reson. Chem.* **2006**, *44*, 573–580. [CrossRef]
12. Lu, H.B.; Campbell, C.T.; Graham, D.J.; Ratner, B.D. Surface characterization of hydroxyapatite and related calcium phosphates by XPS and TOF-SIMS. *Anal. Chem.* **2000**, *72*, 2886–2894. [CrossRef]
13. Young, R.A.; Elliott, J.C. Atomic-scale bases for several properties of apatites. *Arch. Oral Biol.* **1966**, *11*, 699–707. [CrossRef]

14. Veselinovic, L.; Karanovic, L.; Stojanovic, Z.; Bracko, I.; Markovic SIgnatovic, N.; Uskokovic, D. Crystal structure of cobalt-substituted calcium hydroxyapatite nanopowders prepared by hydrothermal processing. *J. Appl. Cryst.* **2010**, *43*, 320–327. [CrossRef]
15. Elliott, J.C.; Wilson, R.M.; Dowker, S.E.P. Apatite structures. *Adv. X-ray Anal.* **2002**, *45*, 172–181.
16. Heimann, R.B. *Plasma Spray Coating. Principles and Applications*, 2nd ed.; Wiley-VCH: Weinheim, Germany, 2008; p. 34.
17. Kreidler, E.R.; Hummel, F.A. Phase relations in the system SrO-P_2O_5 and the influence of water vapor on the formation of $Sr_4P_2O_9$. *Inorg. Chem.* **1967**, *6*, 884–891. [CrossRef]
18. Alberius-Henning, P.; Adolfson, E.; Grins, J.; Fitch, A. Triclinic oxy-hydroxyapatite. *J. Mater. Sci.* **2001**, *36*, 663–668. [CrossRef]
19. Liao, C.J.; Lin, F.H.; Chen, K.S.; Sun, J.S. Thermal decomposition and reconstruction of hydroxyapatite in air atmosphere. *Biomaterials* **1999**, *20*, 1807–1813. [CrossRef]
20. Trombe, J.C.; Montel, G. Sur la preparation de l'oxyapatite phosphocalcique. *Comptes Rendus Séances l'Académie Sci. (Paris) Série C* **1971**, *273*, 452–465.
21. Hartmann, P.; Jäger, C.; Barth, S.; Vogel, J.; Meyer, K. Solid state NMR, X-ray diffraction, and infrared characterization of local structure in heat-treated oxyhydroxylapatite microcrystals: An analogy of the thermal deposition of hydroxyapatite during plasma-spray procedure. *J. Solid State Chem.* **2001**, *160*, 460–468. [CrossRef]
22. Heimann, R.B.; Tran, H.V.; Hartmann, P. Laser-Raman and Nuclear Magnetic Resonance (NMR) studies on plasma-sprayed hydroxyapatite coatings: Influence of bioinert bond coats on phase composition and resorption kinetics in simulated body fluid. *Entwickl. Fert. Prüfung Eig. Anwend. Tech. Werkst.* **2003**, *34*, 1163–1169.
23. Kijima, T.; Tsutsumi, M. Preparation and thermal properties of dense polycrystalline oxyhydroxyapatite. *J. Am. Ceram. Soc.* **1979**, *62*, 455–460. [CrossRef]
24. Hendricks, S.B.; Hill, W.A.; Jakobs, K.D.; Jefferson, M.E. Structural characteristics of apatite-like substances and composition of phosphate rock and bone as determined from microscopical and X-ray examinations. *Ind. Eng. Chem.* **1931**, *23*, 1413–1418. [CrossRef]
25. Voelcker, J.A. Die chemische Zusammensetzung des Apatits nach eigenen vollständigen Analysen. *Ber. Dtsch. Chem. Ges.* **1883**, *16*, 2460–2464. [CrossRef]
26. Rogers, A.F. A new locality for voelckerite and the validity of voelckerite as a mineral species. *Mineral. Mag. J. Mineral. Soc.* **1914**, *17*, 155–162. [CrossRef]
27. Bredig, M.A.; Franck, H.H.; Füldner, H. Beiträge zur Kenntnis der Kalk-Phosphorsäure-Verbindungen II. *Z. Für Elektrochem. Angew. Phys. Chem.* **1933**, *39*, 959–969.
28. De Leeuw, N.; Bowe, J.R.; Rabone, J.A.L. A computational investigation of stoichiometric and calcium-deficient oxy- and hydroxyapatite. *Faraday Disc.* **2007**, *134*, 195–214. [CrossRef] [PubMed]
29. McConnell, D.; Hey, M.H. The oxyapatite (voelckerite) problem. *Min. Mag.* **1969**, *37*, 301–303. [CrossRef]
30. Trombe, J.C.; Montel, G. Some features of the incorporation of oxygen in different oxidation states in the apatite lattice. I. On the existence of calcium and strontium oxyapatite. *J. Inorg. Nucl. Chem.* **1978**, *40*, 15–21. [CrossRef]
31. Calderin, L.; Stott, M.J.; Rubio, A. Electronic and crystallographic structure of apatite. *Phys. Rev. B* **2003**, *67*, 134106–134112. [CrossRef]
32. Alberius-Henning, P.; Landa-Canovas, A.; Larsson, A.K.; Lidin, S. The structure of oxyapatite solved by HREM. *Acta Crystallogr. B* **1999**, *55*, 170–176.
33. Gross, K.A.; Berndt, C.C.; Stephens, P.; Dinnebier, R. Oxyapatite in hydroxyapatite coatings. *J. Mater. Sci.* **1998**, *33*, 3985–3991. [CrossRef]
34. Gross, K.A.; Ben-Nissan, B.; Walsh, W.R.; Swarts, E. Analysis of retrieved hydroxyapatite coated orthopaedic implants. In *Thermal Spray. Meeting the Challenges of the 21st Century*; Coddet, C., Ed.; ASM International: Almere, The Netherlands, 1998; pp. 1133–1138.
35. Gross, K.A.; Berndt, C.C. Thermal processing of hydroxyapatite for coating production. *J. Biomed. Mater. Res.* **1998**, *39*, 580–587. [CrossRef]
36. Trombe, J.C. Contribution á l'étude de la decomposition et de la réactivité de certaines apatites hydroxylées et carbonates. *Ann Chim. (Paris)* **1973**, *8*, 335–347.
37. Montel, G.; Bonel, G.; Trombe, J.C.; Heughebaert, J.C.; Rey, C. Progress dans le domaine de la chimie des composes phosphores solides a structure d'apatite. *Pure Appl. Chem.* **1980**, *52*, 973–987. [CrossRef]
38. Heimann, R.B. Characterisation of as-sprayed and incubated hydroxyapatite coatings with high resolution techniques. *Mater. Werkst.* **2009**, *40*, 23–30. [CrossRef]
39. Keller, L.; Dollase, W.A. X-ray determination of crystalline hydroxyapatite to amorphous calcium phosphate ratio in plasma sprayed coatings. *J. Biomed. Mater. Res.* **2000**, *49*, 244–249. [CrossRef]
40. Dickens, B.; Brown, W.E.; Kruger, G.J.; Stewart, J.M. $Ca_4(PO_4)_2O$, tetracalcium diphosphate monoxide. Crystal structure and relationships to $Ca_5(PO_4)_3OH$ and $K_3Na(SO_4)_2$. *Acta Cryst.* **1973**, *29*, 2046–2056. [CrossRef]
41. Posner, A.S.; Perloff, A.; Diorio, A.F. Refinement of the hydroxyapatite structure. *Acta Cryst.* **1958**, *11*, 308–309. [CrossRef]
42. Tas, A.C. X-ray diffraction data for flux-grown calcium hydroxyapatite whiskers. *Powder Diffr.* **2001**, *16*, 102–106. [CrossRef]
43. Elliott, J.C.; Mackie, P.E.; Young, R.A. Monoclinic hydroxylapatite. *Science* **1973**, *180*, 1055–1057. [CrossRef] [PubMed]

44. Yashima, M.; Kawaike, Y.; Tanaka, M. Determination of precise unit cell parameters of the α-tricalcium phosphate $Ca_3(PO_4)_2$ through high-resolution synchrotron powder diffraction. *J. Am. Ceram. Soc.* **2007**, *90*, 272–274. [CrossRef]
45. Yashima, M.; Sakai, A.; Kamiyama, T.; Hoshikawa, A. Crystal structure analysis of ß-tricalcium phosphate $Ca_3(PO_4)_2$ by neutron diffraction. *J. Solid State Chem.* **2003**, *175*, 272–277. [CrossRef]
46. Weinlaender, M.; Beumer, J.I.I.I.; Kenney, E.B.; Moy, P.K.; Adar, F. Raman microprobe investigation of the calcium phosphate phases of three commercially available plasma-flame-sprayed hydroxyapatite-coated dental implants. *J. Mater. Sci. Mater. Med.* **1992**, *3*, 397–401. [CrossRef]
47. Demnati, I.; Parco, M.; Grossin, D.; Fagoaga, I.; Drouet, C.; Barykin, G.; Combes, C.; Braceras, I.; Gonsalves, S.; Rey, C. Hydroxyapatite coating on titanium by a low energy plasma spraying mini-gun. *Surf. Coat. Technol.* **2012**, *206*, 2346–2353. [CrossRef]
48. Heimann, R.B.; Vu, T.A.; Wayman, M.L. Bioceramic coatings: State-of-the-art and recent development trends. *Eur. J. Mineral.* **1997**, *9*, 597–615. [CrossRef]
49. Heimann, R.B. Plasma-sprayed hydroxylapatite coatings as biocompatible intermediaries between inorganic implant surfaces and living tissue. *J. Therm. Spray Technol.* **2018**, *27*, 1212–1237. [CrossRef]
50. Shamray, V.F.; Sirotinkin, V.P.; Kalita, V.I.; Komlev, V.S.; Barinov, S.M.; Fedotov, Y.; Gordeev, A.S. Study of the crystal structure of hydroxyapatite in plasma coating. *Surf. Coat. Technol.* **2019**, *372*, 201–208. [CrossRef]
51. Hartmann, P.; Barth, S.; Vogel, J.; Jäger, C. Investigation of structural changes in plasma-sprayed hydroxyapatite. In *Applied Mineralogy in Research, Economy, Technology, Ecology and Culture*; Rammlmair, D., Mederer, J., Oberthür, T., Heimann, R.B., Pentinghaus, H., Eds.; A.A. Balkema: Rotterdam, The Netherlands, 2000; Volume 1, pp. 147–150.
52. Heimann, R.B. Tracking the thermal decomposition of plasma-sprayed hydroxylapatite. *Am. Mineral.* **2015**, *100*, 2419–2425. [CrossRef]
53. Tran, H.V. Investigation into the Thermal Dehydroxylation and Decomposition of Hydroxyapatite during Atmospheric Plasma Spraying: NMR and Raman Spectroscopic Study of As-Sprayed Coatings and Coatings Incubated in Simulated Body Fluid. Ph.D. Thesis, Department of Mineralogy, Technische Universität Bergakademie Freiberg, Freiberg, Germany, 2004.
54. Heimann, R.B. Novel approaches towards design and biofunctionality of plasma-sprayed osteoconductive calcium phosphate coatings for biomedical implants: The concept of bond coats. In *Trends in Biomaterials Research*; Pannone, P.J., Ed.; Nova Science Publ. Inc.: New York, NY, USA, 2007; pp. 1–80.
55. Kim, H.M.; Miyazaki, T.; Kokubo, T.; Nakamura, T. Revised simulated body fluid. *Bioceramics* **2001**, *13*, 47–50. [CrossRef]
56. Moseke, C.; Gbureck, U. Tetracalcium phosphate: Synthesis, properties and biomedical applications. *Acta Biomater.* **2010**, *6*, 3815–3823. [CrossRef] [PubMed]
57. Nimkerdphol, A.R.; Otsuka, Y.; Mutoh, Y. Effect of dissolution/precipitation on the residual stress distribution of plasma-sprayed hydroxyapatite coating on titanium substrate in simulated body fluid (SBF). *J. Mech. Behav. Biomed. Mater.* **2014**, *36*, 98–108. [CrossRef]
58. Heimann, R.B. *Materials for Medical Application*; Walter De Gruyter GmbH: Berlin, Germany, 2020.
59. US Dept. of Health and Human Services. *FDA Guidance for Industry and FDA Staff: Non-Clinical Information for Femoral Stem Prostheses*; Silver Springs: Marion, FL, USA, 2007.
60. US Dept. of Health and Human Services. *FDA Guidance for Industry and FDA Staff: Root-Form Endosseous Dental Implants and Endosseous Dental Abutments*; Silver Springs: Marion, FL, USA, 2004.
61. Campbell, A.A. Bioceramic for implant coating. *Mater. Today* **2003**, *11*, 26–30. [CrossRef]
62. Heimann, R.B.; Lehmann, H.D. *Bioceramic Coatings for Medical Implants. Trends and Techniques*; Wiley-VCH: Weinheim, Germany, 2015.
63. *ASTM F1185-03(2014) Standard Specification for Composition of Hydroxylapatite for Surgical Implants*; ASTM International: West Conshohocken, PA, USA, 2014; Available online: https://www.astm.org (accessed on 2 July 2021).
64. *ASTM F1609-08(2014) Standard Specification for Calcium Phosphate Coatings for Implantable Materials*; ASTM International: West Conshohocken, PA, USA, 2014; Available online: https://www.astm.org (accessed on 2 July 2021).
65. *ISO 13779-2:2008 Implants for Surgery-Hydroxyapatite. Part 2: Coatings of Hydroxyapatite*; International Organization for Standardization [ISO]: Geneva, Switzerland, 2008; Available online: https://commitee.iso.org (accessed on 25 June 2021).
66. Pasteris, J.D.; Wopenka, B.; Freeman, J.J.; Rogers, K.; Valsami-Jones, E.; van der Houwen, J.A.M.; Silva, M.J. Lack of OH in nanocrystalline apatite as a function of degree of atomic order: Implications for bone and biomaterials. *Biomaterials* **2004**, *25*, 229–238. [CrossRef]
67. Wopenka, B.; Pasteris, J.D. A mineralogical perspective on the apatite in bone. *Mater. Sci. Eng. C* **2005**, *25*, 131–143. [CrossRef]
68. Chen, J.H.; Chao, L.; You, L.D.; Simmons, C.A. Boning up on Wolff's Law: Mechanical regulation of the cells that make and maintain bone. *J. Biomech.* **2010**, *43*, 108–118. [CrossRef] [PubMed]
69. Heimann, R.B. Functional plasma-sprayed hydroxylapatite coatings for medical application: Clinical performance requirements and key property enhancement. *J. Vac. Sci. Technol.* **2021**, *39*. in press. [CrossRef]
70. Surmenev, R.A.; Surmeneva, M.A.; Ivanova, A.A. Significance of calcium phosphate coatings for the enhancement of new bone osteogenesis—A review. *Acta Biomater.* **2014**, *10*, 557–579. [CrossRef]
71. Gittens, R.A.; Olivares-Navarrete, R.; Schwartz, Z.; Boyan, B.D. Implant osseintegration and the role of microroughness and nanostructures: Lessons for spine implants. *Acta Biomater.* **2014**, *10*, 3363–3371. [CrossRef]